

# Visualising How Non-linear Dimension Reduction Warps Your Data

Jayani P.G. Lakshika

Econometrics & Business Statistics, Monash University  
and

Dianne Cook

Econometrics & Business Statistics, Monash University  
and

Paul Harrison

MGBP, BDInstitute, Monash University  
and

Michael Lydeamore

Econometrics & Business Statistics, Monash University  
and

Thiyanga S. Talagala

Statistics, University of Sri Jayewardenepura

March 18, 2024

## Abstract

Non-Linear Dimension Reduction (NLDR) techniques have emerged as powerful tools to visualize high-dimensional data. However, their complexity and parameter choices may lead to distrustful or misleading results. To address this challenge, we propose a novel approach that combines the tour technique with a low-dimensional manifold generated using NLDR techniques, hexagonal binning, and triangulation. This integration enables a clear examination of the low-dimensional representation in the original high-dimensional space. Our approach not only preserves the advantages of both tours and NLDR but also offers a more intuitive perception of complex data structures and facilitates accurate data transformation assessments. The method and example data sets are available in the **quollr** R package.

*Keywords:* high-dimensional data, dimension reduction, triangulation, hexagonal binning, low-dimensional manifold, manifold learning, tour, data visualization

# 1 Introduction

High-dimensional (high-D) data is prevalent across various fields, such as ecology and bioinformatics (Guo et al. 2023), due to advancements in data collection technologies (Johnstone & Titterington 2009, Ayesha et al. 2020). However, visualization of high-D data introduces significant challenges, because the complexity of visualizing data beyond two dimensions (Jia et al. 2022). In recent years, interactive and dynamic graphics systems like **liminal** (Lee et al. 2020)—which employs interactive tools like brushing and linking (Wickham et al. 2015)—and software tools such as **XGobi**, **GGobi** (Swayne et al. 1998), **tourr** (Wickham et al. 2011), **detourr** (Hart & Wang 2022), and **langevitour** (Paul Harrison 2022), involving dynamic methods like tours (Asimov 1985), have played a key role in visualizing high-D data (data-vis).

To create low-dimensional representations (typically in 2D) (m-vis) (Buja et al. 1996) of high-D data, it is common to apply dimension reduction (DR) techniques. Approaches for DR involve linear methods such as principal component analysis (PCA) (F.R.S. 1901), non-linear methods such as multi-dimensional scaling (MDS) (Torgerson 1967). In the past decade, many new non-linear dimension reduction (NLDR) techniques have emerged, such as t-distributed stochastic neighbor embedding (tSNE) (van der Maaten & Hinton 2008) and uniform manifold approximation and projection (UMAP) (McInnes & Healy 2018). NLDR techniques are the 2D models of high-D data in our context.

It is important to visualize various non-linear dimensionality reduction (NLDR) techniques for the same high-D data in order to understand and find the best representation. After doing so, the 2D models may differ considerably from each other and may also deviate from the original data structure in high-dimensional space. Therefore, visualizing the 2D model in high-D space (m-in-ds) is more useful to answer different types of questions:

- Is there a best 2D representation of high-D data or are they all providing equivalent information? Is there a best parameter choice to fit the 2D model? How does the model change when its parameters change?
- How well does the 2D models capture the data structure? Is the model fitting able to capture different data structure like non-linear, clustering?

If we cannot easily ask and answer these questions, our ability to understand the models is limited. To find the best 2D model and parameter choices, a better understanding of the underlying science is important.

Also, the importance of m-vis along with data-vis has been recognized and incorporated into interactive software, **liminal** (Lee et al. 2020). But the 2D model and high-D visualize side by side and interactive like brushing and linking connect the data in the two panels. To address this challenge, we propose a novel approach by combining the tour technique with a low-dimensional manifold. This manifold is created through the synergistic use of NLDR techniques, hexagonal binning, and triangulation. This integration facilitates a more understanding of the data structure, how well (or how poorly) NLDR techniques perform.

The outline of this paper is as follows. The Section 2 provides an detailed overview of dimension reduction methods, and tours. Building upon this foundation, the Section 3

delves into the proposed algorithm, its implementation details, how to tune the model, model summaries, and a synthetic example to illustrate the functionality of the algorithm. Subsequently, Section 4 showcases applications of the algorithm on different data sets, particularly in single-cell RNA-seq data. These applications reveal insights into the performance and trustworthiness of NLDR algorithms. We analyze the results to identify situations where NLDR techniques may lead to misleading interpretations. Finally, ?@sec-conclusions concludes by summarizing the findings and emphasizing the significance of the proposed approach in tackling the challenges of high-dimensional data visualization.

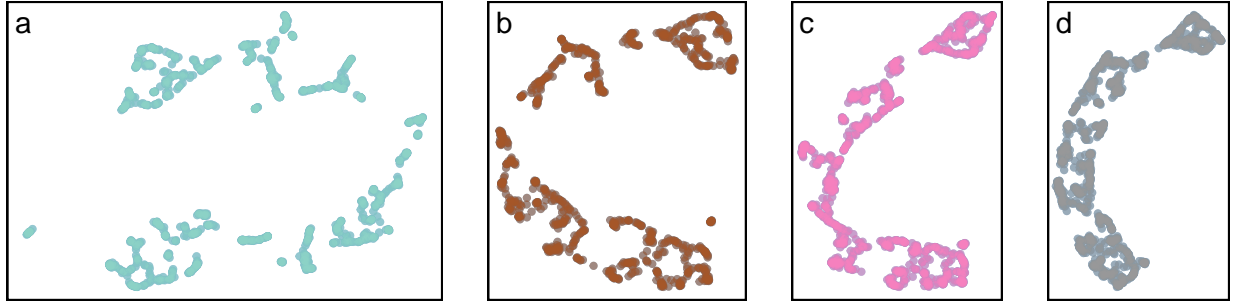


Figure 1: 2D layouts from UMAP applied for the S-curve data: (a) UMAP ( $n_{\text{neighbors}} = 7$ ), (b) UMAP ( $n_{\text{neighbors}} = 15$ ), (c) UMAP ( $n_{\text{neighbors}} = 32$ ), (d) UMAP ( $n_{\text{neighbors}} = 50$ ). Is there a best hyperparameter choice in representing UMAP or are they all providing equivalent information?

## 2 Background

### 2.1 Dimension Reduction

Consider the high-D data a rectangular matrix  $X_{n \times p}$ , where  $X_{n \times p} = [\mathbf{x}_1 \ \mathbf{x}_2 \ \cdots \ \mathbf{x}_n]^{\top}$ , with  $n$  observations in  $p$  dimensions. The objective is to discover a low-dimensional projection  $Y_{n \times d} = [\mathbf{y}_1 \ \mathbf{y}_2 \ \cdots \ \mathbf{y}_n]^{\top}$ , represented as an  $n \times d$  matrix, where  $d \ll p$ . The reduction process seeks to remove noise from the original data set while retaining essential information.

There are two main categories of dimension reduction techniques: linear and non-linear methods. Linear techniques involve a linear transformation of the data, with one popular example being PCA. PCA performs an eigen-decomposition of the sample covariance matrix to obtain orthogonal principal components that capture the variance of the data (F.R.S. 1901).

In contrast, NLDR techniques generate the low-dimensional representation  $Y$  from the high-dimensional data  $X$ , often using pre-processing techniques like  $k$ -nearest neighbors graph or kernel transformations. Multidimensional Scaling (MDS) is a class of NLDR methods that aims to construct an embedding  $Y$  in a low-dimensional space, approximating the pair-wise distances in  $X$  (Torgerson 1967). Variants of MDS include non-metric scaling (Kruskal 1964) and Isomap, which estimate geodesic distances to create the low-dimensional representation (Silva & Tenenbaum 2002). Other approaches based on diffusion processes, like diffusion maps (Coifman et al. 2005) and the PHATE (Potential of Heat-diffusion for

Affinity-based Trajectory Embedding) algorithm ([Moon et al. 2019](#)), also fall under NLDR methods.

### 2.1.1 Non-linear dimension reduction techniques

NLDR techniques are crucial for analyzing and displaying high-dimensional data, where linear approaches may not adequately capture complexities in relationships between variables ([Johnstone & Titterington 2009](#)). One of the challenges with NLDR techniques is the selection and tuning of appropriate hyperparameters ([Liao et al. 2023](#)). This process involves finding the suitable combination of hyperparameters that enhances the performance of the NLDR technique, considering the characteristics of the dataset and the specific goals of the analysis.

Additionally, another challenge is lack of reverse mapping. Techniques like PCA and auto-encoders ([Rumelhart et al. 1986](#)) provide a way to map back from the low-dimensional space to the high-D space, facilitating data reconstruction. However, some NLDR methods, such as tSNE, don't have a specific way to reconstruct the original data from the low-dimensional space.

In this article, mainly focus on five NLDR techniques. They are tSNE, UMAP, PHATE, TriMAP ([Amid & Warmuth 2022](#)), and Pairwise Controlled Manifold Approximation (PaCMAP) ([Wang et al. 2021](#)).

Among these, tSNE ([van der Maaten & Hinton 2008](#)) stands out for its ability to preserve pairwise distances. By minimizing the divergence between probability distributions in both high and low-dimensional spaces, tSNE effectively uncovers intricate structures and patterns within the data. Its application is widespread, particularly in tasks requiring the visualization of clusters and local relationships. However, achieving effective results requires careful consideration of hyperparameters, such as perplexity.

UMAP ([McInnes & Healy 2018](#)) is a useful technique for simplifying data while maintaining both local and overall structures. It builds a fuzzy topological view by considering nearby data points and then optimizes a simplified version to match that view. UMAP is known for working well with different scales of relationships in data and is efficient in handling large datasets. However, it's important to choose parameters like neighbors and minimum distance carefully, as they can affect the results.

Furthermore, PHATE ([Moon et al. 2019](#)) is great for understanding how things develop, especially in single-cell genomics. It uses a heat diffusion process to capture relationships between data points, like points along a trajectory. While PHATE is excellent for revealing these developmental structures, it requires careful tuning of its parameters because of its specialized focus.

Additionally, TriMAP ([Amid & Warmuth 2022](#)) takes a special approach by creating a triangulated graph representation of the data. This method is good at understanding both local and global structures by treating the data as a network of triangles. TriMAP is powerful in capturing complicated structures, but it's important to choose parameters carefully, like deciding how many neighbors to consider.

PaCMAP ([Wang et al. 2021](#)) is different because it adds supervised learning to make a

2D representation while keeping the relationships between pairs of points. It builds a graph using distances between pairs and then makes the 2D representation better using a customizable loss function. What’s special about PaCMAP is that it can use class labels or extra information to guide how it makes the 2D representation. This gives users a way to change how PaCMAP works to fit their needs better.



Figure 2: 2D layouts from different NLDR techniques applied the same data: (a) tSNE (perplexity = 27), (b) UMAP (n\_neighbors = 50), (c) PHATE (knn = 5), (d) TriMAP (n\_inliers = 5, n\_outliers = 4, n\_random = 3), and (e) PaCMAP (n\_neighbors = 10, init = random, MN\_ratio = 0.9, FP\_ratio = 2). Is there a best representation of the original data or are they all providing equivalent information?

## 2.2 Linear overviews using tours

A tour is a powerful visualization technique used to explore the shape and global structure of high-dimensional data by generating a sequence of projections, typically into two dimensions. There are two main types of tours: the grand tour (Asimov 1985) and the guided tour (Cook et al. 1995). A grand tour involves randomly selecting new orthonormal bases, enabling users to understand the structure by exploring the subspace of d-dimensional projections (Asimov 1985). In contrast, a guided tour can be employed to generate a sequence of ‘interesting’ projections based on an index function (Cook et al. 1995).

The process begins with the data matrix  $X$ . It generates a sequence of  $p \times d$  orthonormal projection matrices (bases)  $P_t$ , usually  $d$  is one or two dimensions. For each pair of orthonormal bases  $P_t$  and  $P_{t+1}$ , a geodesic path is interpolated to create smooth animation between projections. The resulting tour continuously visualizes the projected data  $Y_t = X P_t$  as it interpolates between successive bases.

Furthermore, software like **langevitour** can visualize both types of tours, providing flexibility for exploring high-dimensional data with various objectives. In our context, use grand tour along with the model to observe how effectively the model captures the underlying structure of the data.

## 3 Methodology

In this paper, we introduce a novel method to determine the most effective NLDR technique and the best hyperparameter choice that provides the most useful representation of high-D data. Our approach involves dividing the high-D dataset into two parts: a training set for constructing the model and a test set for generating predictive values and residuals. Our

algorithm takes a 2D embedding data as the input and generate a tour that displays the high-D wireframe to overlay the data. The flow chart of the proposed algorithm is shown in Figure 3. The algorithm consists of two main phases: (1) generating the model in the 2D space and (2) lifting the model into high-D space. The main steps of the algorithm are described in detail in this section using UMAP 2D embedding of the S-curve dataset. This dataset has seven dimensions, including four noise dimensions that were added to the original 3D data.



Figure 3: The flow diagram shows the main steps of our algorithm. There are two basic phases, one to generate the model in the 2D space, and other to map the model into the high-D space.

### 3.1 Preprocessing steps

To reduce computational complexity when applying NLDR techniques to high-D data and to reduce noise presence, PCA ([Jolliffe & Cadima 2016](#), [Howley et al. \(2005\)](#), [Indhumathi & Sathiyabama \(2010\)](#)) is used as a preprocessing step. PCA involves identifying principal components that maximize variance. These components are then used as the high-D data for the algorithm.

## 3.2 Constructing the 2D model

### Step 1: Scaling NLDR data

First, we prepare the 2D embedding data to fit within the bounds required for regular hexagonal binning. To achieve this, we implement two key scaling steps. Scale the first 2D embedding component to range between 0 and 1, ensuring that all data points fall within this normalized interval. Secondly, we scale the second 2D embedding component to range between 0 and  $y_{max}$  (see Equation 3).

The calculation of  $y_{max}$  involves several steps. First, the aspect ratio ( $ar$ ) is computed by dividing the range of the second 2D embedding component ( $r_2$ ) by the range of the first 2D embedding component ( $r_1$ ) (see Equation 1). Then, the hexagon ratio ( $hr$ ) is determined by dividing the height of the hexagon ( $hb$ ) by its width ( $wb$ ) (see Equation 2). Finally,  $y_{max}$  is derived by taking the ceiling of  $\frac{ar}{hr}$  and multiplying it by  $hr$ . This process ensures that  $y_{max}$  is an integer multiple of  $hr$ , accommodating the grid layout of the hexagonal bins.

$$ar = \frac{r_2}{r_1} \quad (1)$$

$$hr = \frac{hb}{wb} \quad (2)$$

$$y_{max} = \left\lceil \frac{ar}{hr} \right\rceil * hr \quad (3)$$

### Step 2: Hexagonating NLDR data

Hexagonating NLDR data (see Figure 3 Step 2) involves partitioning the 2D embedding data into hexagonal bins, a technique commonly referred to as hexagonal binning (Carr et al. 1987, Carr (1992)). This method uses a hexagonal grid to create a bivariate histogram that effectively visualizes the structure of high-D data. Hexagons, one of only three regular polygons capable of tessellating a plane (Carr et al. 2013), offer unique advantages due to their symmetry of nearest neighbors and maximal number of sides for such tessellations (Carr et al. 2023). This geometric property makes hexagons more efficient in covering the plane compared to other regular tessellations and reduces visual bias when displaying data densities (Carr et al. 2023). In our algorithm, we aim to conduct regular hexagonal binning (cite quollr paper), involving the computation of hexagonal grid configurations, the generation of the grid, and the assignment of the 2D embedding to hexagons.

### Step 3: Obtaining bin centroids or bin means

In the previous step, the algorithm clusters the 2D embedding data into hexagons. Following this, in this step, the bin centroids or bin means (see Figure 3 Step 3) are obtained (Carr et al. 2013).

The bin centroid ( $C_k^{(2)}$ ) for a  $k^{th}$  hexagon with hexagonal grid coordinates  $(h^k x_i, h^k y_i)$ , where  $i = 1 \dots 6$  can be defined as:

$$C_k^{(2)} = (C_{ky_1}, C_{ky_2}) = \left( \frac{\sum_{i=1}^6 h^k x_i}{6}, \frac{\sum_{i=1}^6 h^k y_i}{6} \right). \quad (4)$$

Also, the bin mean ( $C_k^{(2)}$ ) is defined as the mean of the data points within the  $k^{th}$  hexagon (see Equation 5).

$$C_k^{(2)} = (C_{ky_1}, C_{ky_2}) = \left( \frac{1}{n_k} \sum_{i=1}^{n_k} y_{1i}, \frac{1}{n_k} \sum_{i=1}^{n_k} y_{2i} \right), \quad (5)$$

where  $n_k$  is the number of data points within the hexagon,  $y_{1i}$  and  $y_{2i}$  are the  $x$  and  $y$  coordinates of the  $i^{th}$  data point within the hexagon.

#### Step 4: Triangulating bin centroids or bin means

In this step, the algorithm proceeds to triangulate the hexagonal bin centroids or bin means (see Figure 3 Step 4). Triangulation is a fundamental process in computational geometry and computer graphics that involves dividing a set of points in a given space into interconnected triangles (Lloyd 1977). One common algorithm used for triangulation is Delaunay triangulation (Lee & Schachter 1980, Renka (1996)), where points are connected in a way that maximizes the minimum angles of the resulting triangles, leading to a more regular and well-conditioned triangulation.

Delaunay triangulation can be defined as follows:

Let  $C^{(2)} = \{C_1^{(2)}, C_2^{(2)}, \dots, C_m^{(2)}\}$  be a set of  $m$  bin centroids or bin means in the plane. Delaunay triangulation of  $C^{(2)}$ , denoted as  $DT(C^{(2)})$ , is a triangulation of the convex hull of  $C^{(2)}$  such that the circumcircle of every triangle in the triangulation contains no other points from  $C^{(2)}$ .

Given that the hexagons are regular, the resulting triangles will mostly be equilateral.

### 3.3 Lifting the model into high dimensions

#### 3.3.1 Lifting the triangular mesh points into high dimensions

Consider  $f : \mathbb{R}^p \rightarrow \mathbb{R}^2$  be a function that maps the high-D data ( $X_{n \times p}$ ) to its NLDR equivalent ( $Y_{n \times d}$ ). Then, let  $g : \mathbb{R}^2 \rightarrow \mathbb{R}^2$  be a function that maps each 2D embedding point to its closest centroid ( $C^{(2)}$ ). It follows that  $f(g(x))$  maps the high-D points  $x$  to the centroid in 2D ( $C_k^{(2)}$ ). Also, define a function  $v : \mathbb{R}^2 \rightarrow \mathbb{R}^p$  maps the 2D centroid ( $C^{(2)}$ ) to the high-D mean of the points ( $C^{(p)}$ ) in the hexagon.

The high-D mean of all the points in  $k^{th}$  hexagon by

$$C_k^{(p)} = (C_{kx_1}, \dots, C_{kx_p}) = \left( \frac{1}{n_k} \sum_{i=1}^{n_k} x_{1i}, \frac{1}{n_k} \sum_{i=1}^{n_k} x_{2i}, \dots, \frac{1}{n_k} \sum_{i=1}^{n_k} x_{pi} \right). \quad (6)$$

Therefore,

$$v(C_k^{(2)}) = C_k^{(p)}. \quad (7)$$

Therefore,  $f(g(x))$  gives the 2D centroid associated with high-D points  $x$ , and  $v(C_k^{(2)})$  gives the high-D centroid associated with 2D point  $C_k^{(2)}$ . Thus,  $v(f(g(x)))$  gives the high-D centroid ( $C_k^{(p)}$ ) associated with the 2D embedding of the points  $x$ .

### 3.3.2 Lifting the 2D triangular mesh into high dimensions

As described in Step 4 of Section 3.2, during the triangulation process in 2D space, vertices are identified to form edges. With the knowledge of the high-D mappings for the 2D hexagonal bins, the vertices connected in 2D are also connected in high-D (see video linked in [?@fig-wkhighD](#)).

## 3.4 Tuning the model

The performance and robustness of our model depend on four key parameters: (i) the total number of bins ( $b$ ), (ii) a benchmark value used to remove low-density hexagons, (iii) a benchmark value used to remove long edges, and (iv) starting point of the hexagonal grid. However, there is no analytical formula to calculate an appropriate value for these parameters (the computation of default values can be found in *quollr* paper). The selection of these parameter values depends on the model performance computed by Mean Squared Error (MSE) (see Section 3.5.2).

### 3.4.1 Total number of bins

The number of hexagonal bins in the hexagonal grid has a considerable impact on the construction of the 2D model. This is because it is the initial step in building the 2D model. The hexagonal grid with the chosen total number of bins must be able to capture the structure of the NLDR data. If the number of bins is too low, the model may not be able to capture the structure of the NLDR data effectively (see [?@fig-binsize \(a\)](#)), while if there are too many bins, it may result in over-fitting the individual points of the NLDR data (see [?@fig-binsize \(c\)](#)). Therefore, it is important to determine an appropriate number of bins to build an effective model.

$$b = b_1 \times b_2 \quad (8)$$

Furthermore, the total number of bins is determined by the number of bins along the x-axis and y-axis (see Equation 8). To calculate the effective total number of bins, candidate values are selected based on the range between the minimum and approximate maximum number of bins along the x and y axes. The minimum number of bins along each axis is set to 1, while the maximum number is estimated by taking the square root of the NLDR data point count. The analysis evaluates the MSE across varying total bin counts within this range, covering the minimum to maximum values along both axes.

The analysis focuses on exploring the effect of total number of bins on MSE. It considers MSE across different total number of bins, covering the range calculated from the minimum to maximum values along both x and y axes.

Typically, the MSE plot tends to have a steep slope at the beginning, indicating that a smaller number of bins causes a larger amount of error. Then, the slope gradually declines or levels off, indicating that a higher number of bins generates a smaller error. This MSE plot is useful in determining the effective number of bins required to construct the 2D model. Figure 4 (b) has created a graph that shows how the Mean Squared Error (MSE) changes depending on the number of bins assigned in the hexagonal grid for UMAP applied to the S-curve dataset. As per the rule of thumb mentioned earlier, the effective number of bins is determined to be 84, with 6 bins along the x-axis and 14 bins along the y-axis. Furthermore, Figure 5 shows the 2D model constructed using UMAP with the selected total number of bins and how the model overlay on high-D data.

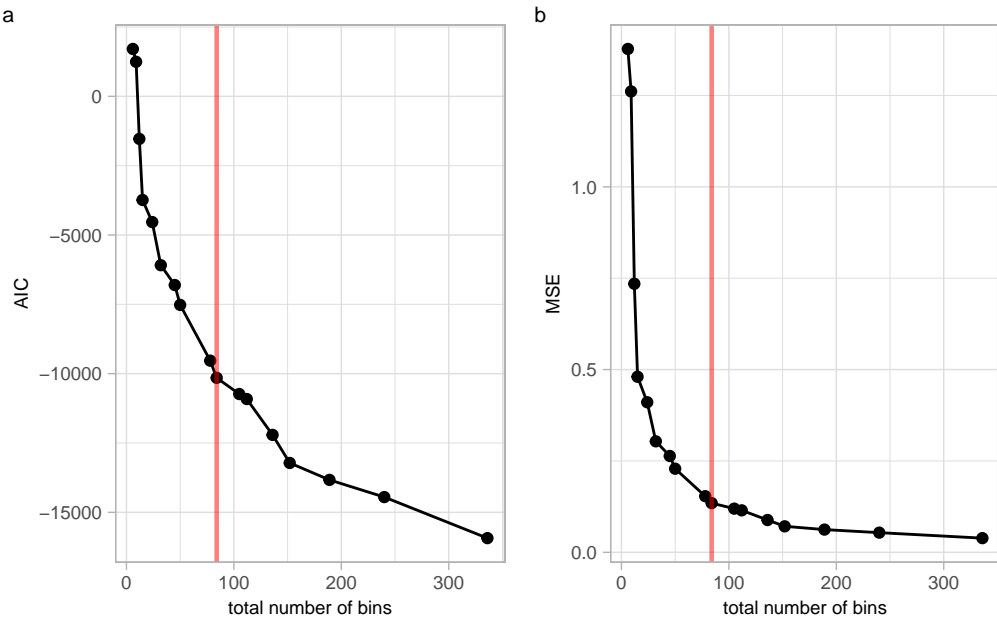


Figure 4: Goodness of fit statistics from UMAP applied to training S-curve dataset. What is the effective number of bins in each NLDR technique to create a 2D model? The MSE plot have a steep slope at the beginning, indicating that a smaller number of bins causes a larger amount of error. Then, the slope gradually declines or level off, indicating that a higher number of bins generates a smaller error. Using the elbow method, when the total number of bins is set to 84, the slope of the Mean Squared Error (MSE) plot experiences a sudden and noticeable change, resembling an elbow-like shape. This point indicates that adding less bins does not enough to capture the data structure.

### 3.4.2 Benchmark value to remove low-density hexagons

After setting up the hexagonal grid with an appropriate number of bins, it is possible that some hexagonal bins may have very few or no data points within them. To ensure comprehensive coverage of the NLDR data, it is necessary to select hexagonal bins that have a considerable number of data points within their hexagons. To achieve this, the

standard number of points within each hexagon is first calculated. This standard count is obtained by dividing the number of points within each hexagon by the maximum number of points in the grid (see Equation 9). Next, the bins that have a standard number of points less than a certain benchmark value are removed. After removing the hexagons that have insufficient data density, the hexagons with more substantial data representation are used to construct the 2D model.

$$\text{standard count} = \frac{\text{count}}{\max \text{ count}} \quad (9)$$

Furthermore, it is crucial to choose the benchmark value to remove low-density hexagons carefully. If we remove unnecessary bins, then it may result in long edges and an uneven 2D model. Therefore, instead of removing hexagons only identified by the benchmark value, we examine the standard number of points in the neighboring hexagons of the identified low-density hexagons. If the neighboring bins also have low counts, then only those bins will be removed. The other identified bins will be kept and used for constructing the 2D model along with the high-density bins (see Appendix for more details).

The benchmark value for removing low-density hexagons has a range of 0 and 1. When analyzing how these benchmark values affect model performance, it's important to observe the change in Mean Squared Error (MSE) as the benchmark value increases. The MSE exhibits a gradual increase as the benchmark value progresses from 0 to 1. Assessing this rate of increase is crucial. If the increment is not substantial, the decision might lean towards retaining low-density hexagons. According to `?@fig-diagnosticpltScurveLwd`, the change in MSE for NLDR techniques is relatively small across different benchmark values, except for the PHATE method.

Consequently, it is not necessary to remove low-density hexagons when constructing the 2D model for the S-curve dataset in NLDR techniques, except for PHATE. While there may be some fluctuations in MSE between benchmark values of 0 to 1, the absence of significant changes suggests that maintaining low-density hexagons is preferable. However, to choose the best selection, it's recommended to examine the benchmark values around the first local minimum in the MSE curve. However, the MSE for PHATE fluctuates when benchmark values range between 0 and 1. Therefore, it is necessary to explore the benchmark values surrounding the first local minimum to determine an effective benchmark value. There is no universal rule for selecting a process. As shown in `?@fig-diagnosticpltScurveLwd`, the MSE values for PHATE fluctuate, and the first local minimum is at 0. Therefore, nearby benchmark values such as 0.01, 0.04, and 0.06 were explored to identify the best value for preserving the data structure. In this case, a benchmark value of 0.06 was chosen. The resulting 2D model is shown in Figure 5 (c), while the video link provides a visual representation of how the model appears in high-D.

The following steps will help to find a suitable value to remove low density hexagons:

1. Plot the distribution of the standardized counts
2. See the distribution of counts
3. Take the first quartile

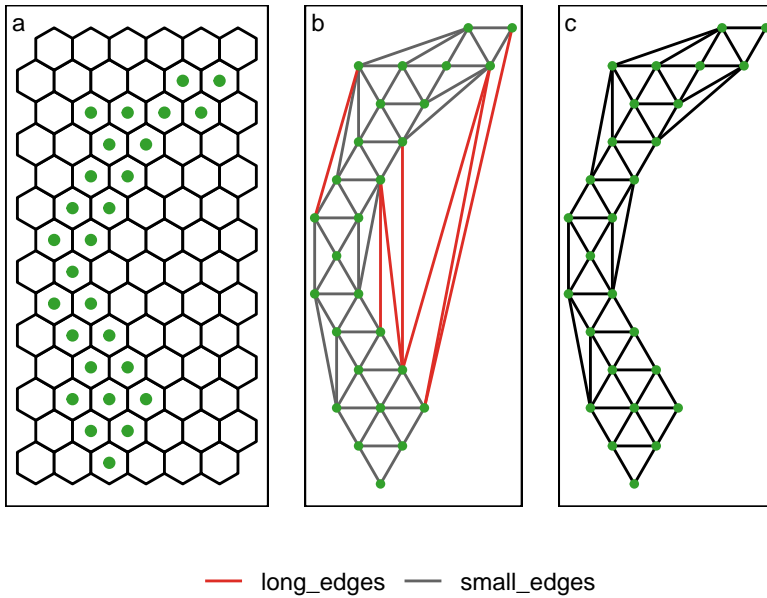


Figure 5: (a), (b) 2D model.

### 3.4.3 Benchmark value to remove long edges

Achieving a smooth representation in 2D space is crucial, and one factor influencing this smoothness is the presence of long edges (see [?@fig-modelScurveMlgimp](#)). These long edges occur when a line connects points that are distant in the triangular mesh, impacting the overall smoothness of the mesh.

To investigate the effect of removing long edges on the MSE, we analyzed the MSE for various benchmark values. Surprisingly, the results indicated that the MSE remained consistent across different benchmark values, as shown in [?@fig-diagnosticpltScurveLgrm](#). It's important to note that edges are defined only in the 2D model and do not extend to higher dimensions. Consequently, removing edges does not affect the model in higher dimensions.

There is no definitive rule for determining the benchmark value to remove long edges. However, we have a method to find a default value (see Appendix). Adjusting values around this default can help to find benchmark value to remove long edges, contributing to the construction of a smoother 2D representation (see [?@fig-diagnosticpltScurveLgrm](#)).

The following steps will help to find a suitable value to remove long edges:

1. Plot the distribution of the 2D distances
2. Find a value which is greater than smallest value

### 3.4.4 Starting point of the hexagonal grid

According to [Carr et al. \(2023\)](#), the hexagonal binning is done by tessellating the  $xy$  plane over the set  $(\text{range}(x), \text{range}(y))$  (see [?@fig-scurveshifthexgridsexp](#) (b)). In that case, bin centroids are defined as shown in [?@fig-scurveshifthexgridsexp](#) (a) with gray colour. Rather than sticking to the typical hexagonal grid, introducing a meaningful shift in both

the x and y directions presents an opportunity for an improved 2D model. Therefore, investigating this shift in the hexagonal grid is an important parameter to consider.

As shown in `?@fig-scurveshifthexgrids`, the shifting influences the distribution of points and number of non-empty bins, impacting the resulting 2D model. According to `?@fig-diagnosticpltScurvehexbins`, the 2D model with a total of 144 bins applied to S-curve UMAP data does not require any shifting because the lowest MSE occurs when no shift is introduced.

## 3.5 Model summaries

### 3.5.1 Predicted values and residuals

The prediction approach involves performing the K-nearest neighbors (KNN) algorithm for an unsupervised classification problem. First, the nearest high-D model point is identified for a given new high-D point. Then, the corresponding 2D centroid mapping for the identified high-D model point is determined. Finally, the coordinates of this 2D centroid are used as the predicted 2D embedding for the new high-D data point. This step is particularly valuable due to the limitations of some NLDR techniques, like tSNE, which don't provide a straightforward method for prediction. As a result, our approach offers a solution that capable of generating predicted 2D embedding regardless of the NLDR technique employed, effectively addressing this functional gap.

Residuals are essential for evaluating the accuracy of representing high-D points by the high-D mapping of 2D bin centroids. To measure this accuracy, an error metric is introduced, quantifying the sum of squared differences between the high-D data ( $x_{ij}$ ) and the high-D mapping of the 2D bin centroid data ( $C_{x_{ij}}$ ) across all observations and dimensions (see Equation 10).

$$\text{Error} = \sum_{j=1}^n \sum_{i=1}^p (x_{ij} - C_{x_{ij}})^2 \quad (10)$$

Here,  $n$  represents the number of observations,  $p$  represents the dimensions of high-D data,  $x_{ij}$  is the high-D data, and  $C_{x_{ij}}$  is the high-D mapping of the 2D bin centroid.

### 3.5.2 Goodness of fit statistics

To assess how well our method captures and represents the underlying structure of the high-D data, Mean Squared Error (MSE) and Akaike Information Criterion (AIC) are used. When computing MSE, total model error (see Section 3.5) is divided by the number of observations to make it as a mean value (see Equation 11).

$$\text{MSE} = \sum_{j=1}^n \frac{\sum_{i=1}^p (x_{ij} - C_{x_{ij}})^2}{n} \quad (11)$$

Furthermore, to incorporate with the parameters in our model, which is the non-empty bins, and as a statistical measure used for model selection and comparison, AIC is used

(see Equation 12).

$$AIC = 2b'p + np * \log(MSE) \quad (12)$$

Here,  $b'$  signifies the number of bins non-empty bins,  $p$  denotes the number of dimensions in the high-D data, and  $n$  represents the number of observations.

### 3.6 Simulated data example

In this section, we showcase the effectiveness of our methodology using simulated data. The dataset comprises five spherical Gaussian clusters in 4-d, with each cluster containing an equal number of points and consistent within variation.

In the 2D representations created by all NLDR techniques, as shown in Figure 6, except for PHATE, there are five distinct clusters. In tSNE, these five clusters are closely located to each other (see Figure 6 (a)). However, in PHATE, two clusters are closely positioned, while the other three are more distant (see Figure 6 (c)). In PaCMAP, one cluster is at the center, and the remaining four are positioned in four different directions (see Figure 6 (e)). In TriMAP, two clusters are close, although not as close as in PHATE, and the other three are well-separated (see Figure 6 (d)). In UMAP, all clusters are arranged in a parallel manner, with three in one line and the other two in a separate line (see Figure 6 (b)).

Visualizing the models alongside the original high-D data provides insights into how different techniques capture the underlying clustering structure. The tSNE model exhibits five well-separated clusters, effectively preserving both local and global structures (see video link of [?@fig-modelfiveGau](#) (a)). UMAP, on the other hand, also presents five distinct clusters but with a more flattened surface appearance (see video link of [?@fig-modelfiveGau](#) (b)). The PHATE model shows five separated clusters resembling triangles or partial triangles but struggles to capture local structures (see video link of [?@fig-modelfiveGau](#) (c)). TriMAP and PaCMAP both display five well-separated clusters with flat surfaces, each capturing within-cluster variation to varying extents. Despite the various 2D representations, all NLDR techniques preserve the global structure (see video link of [?@fig-modelfiveGau](#) (d), (e) respectively). However, tSNE, effectively capture both local and global structures, as indicated by lower AIC values in Figure 7 (a).

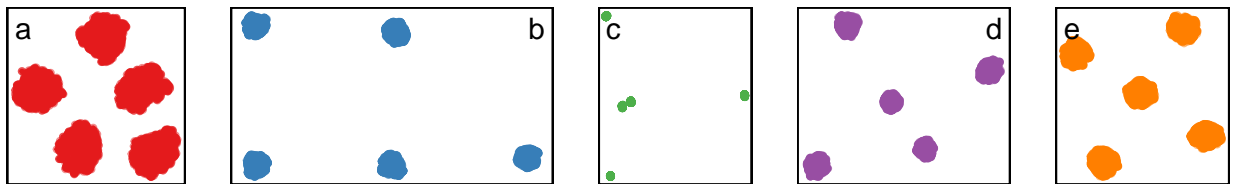


Figure 6: 2D layouts from different NLDR techniques applied the same data: (a) tSNE (perplexity = 61), (b) UMAP (n\_neighbors = 15), (c) PHATE (knn = 5), (d) TriMAP (n\_inliers = 5, n\_outliers = 4, n\_random = 3), and (e) PaCMAP (n\_neighbors = 10, init = random, MN\_ratio = 0.9, FP\_ratio = 2). Is there a best representation of the original data or are they all providing equivalent information?

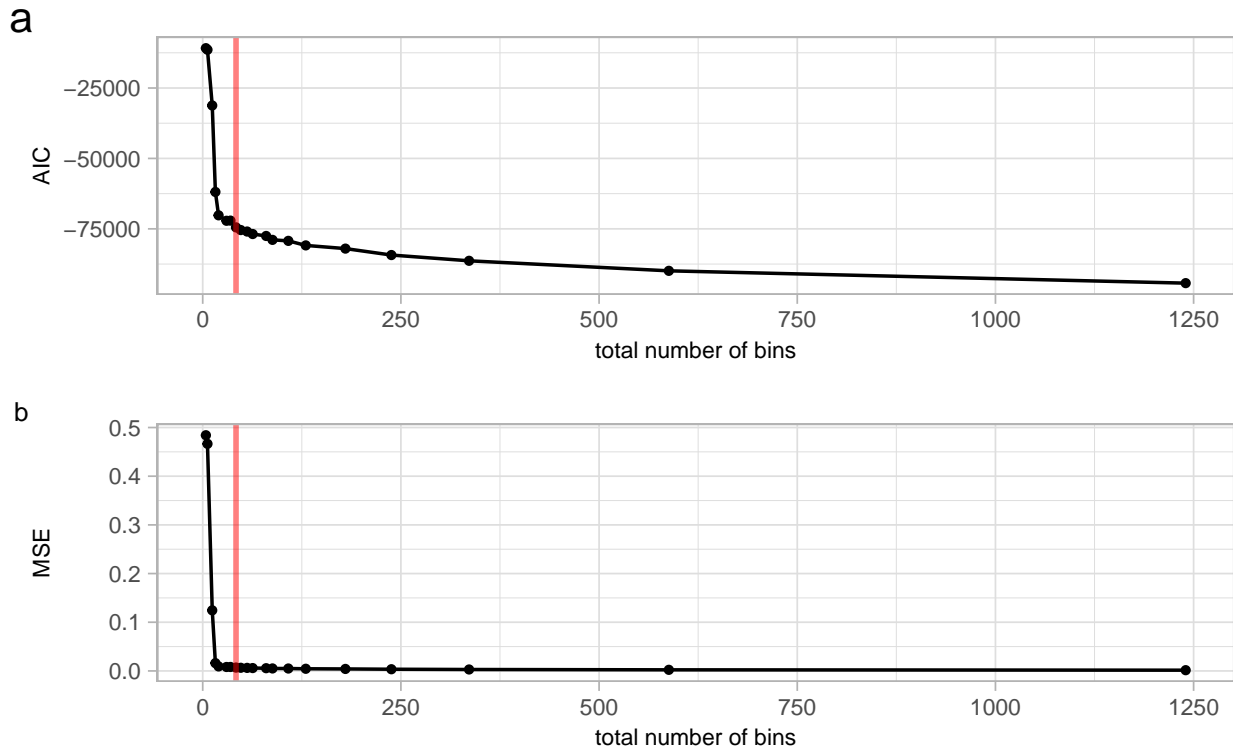


Figure 7: Goodness of fit statistics from different NLDR techniques applied to training five spherical Gaussian cluster dataset. What is the best NLDR technique to represent the original data in 2D?

## 4 Applications

### 4.1 Single-cell RNA-seq data of human

In the field of single-cell studies, a common analysis task involves clustering to identify groups of cells with similar expression profiles. Analysts often turn to NLDR techniques to verify and identify these clusters and explore developmental trajectories. In clustering workflows, the main objective is to verify the existence of clusters and subsequently identify them as specific cell types by examining the expression of “known” marker genes. Marker genes are specific genes or transcripts that are uniquely or highly expressed in particular cell types. Marker genes are identified through differential gene expression (DEG) analysis, comparing the expression levels of genes across different cell types. In this context, a “faithful” embedding should ideally preserve the topology of the data, ensuring that cells corresponding to the same cell type are situated close to the high-dimensional space.

### 4.2 Processing steps

To begin our analysis, we installed the Peripheral Blood Mononuclear Cells (pbmc) data set obtained from 10x Genomics using the `SeuratData` R package ([Satija et al. 2019](#)), which facilitates the distribution of data sets in the form of Seurat objects ([Hao et al. 2021](#)). This data set contains 13,714 features (genes) across 2,700 samples (cells) within a single assay. The active assay is RNA, with 13,714 features representing different gene expressions. Then,

the cells that have unique feature counts over 2,500 or less than 200 and cells that have > 5% mitochondrial counts are filtered. After removing unwanted cells from the dataset, the next step is to normalize the data. By default, we employ a global-scaling normalization method “LogNormalize” that normalizes the feature expression measurements for each cell by the total expression, multiplies this by a scale factor (10,000 by default), and log-transforms the result.

Next, top 1000 genes are selected by Festem ([Chen et al. 2023](#)) DEG method. Then, scale the data. Then, perform PCA on the scaled data. Louvain algorithm is used to cluster the single cells based on the genes selected by Festem. Using the Festem-selected genes and 15 PCs, identified 10 clusters in the PBMC3k data and annotated them based on the expression of canonical markers. The 10 clusters included immune cells such as naive CD4 T cells, memory CD4 T cells, CD8 T cells, CD14 monocytes, FCGR3A monocytes, Natural Killer (NK) cells, B cells and Dendritic Cells (DC). In addition to these common cell types, Festem identified a fine cell type, CD27– CD4+ memory T cells, which were often missed by other methods.

- Human peripheral blood mononuclear cells (PBMCs) data
- Intro to the data set

Used Louvain algorithm to cluster the single cells based on the genes selected by Festem method

- Explain what “Evaluate Festem on DEG detection” means, in terms of this data
- How did they “identified 10 clusters”? What were the variables used, PCs or full data or 2D representation, spell this out.
- Used top 1000 genes selected by Festem to run PCA, top 15 PCs (original paper mentioned)
- The “10 clusters included immune cells such as naive CD4 T ...” does this mean that every cluster had all of these, or one cluster was mostly “CD4 T cells”, another mostly “memory CD4 T”, ...?
- How is your use of this data different from the original application.
- Original paper used this data set to compare different DEG methods, but we need to look how the performance of UMAP with the author’s selected parameter choice.
- Why 15 PCs? Is that from the original paper? YES

### [Chen et al. \(2023\)](#)

- Intro to the data set (This data set contains 13,714 features across 2,700 samples within a single assay. The active assay is RNA, with 13,714 features representing different gene expressions.)
- 2622 cells
- Evaluate Festem on DEG detection (Festem enabled identification of often-missed fine cell types)

- Using the Festem-selected genes, identified 10 clusters in the PBMCsk data and annotated them based on the expression of canonical markers
- The 10 clusters included immune cells such as naive CD4 T cells, memory CD4 T cells, CD8 T cells, CD14 monocytes, FCGR3A monocytes, Natural Killer (NK) cells, B cells and Dendritic Cells (DC).
- In addition to these common cell types, Festem identified a fine cell type, CD27–CD4+ memory T cells, which were often missed by other methods.
- The CD27–CD4+ memory T cells identified by Festem expressed common marker genes (IL7R and S100A4) of memory T cells, but did not express CD27. These cells also had downregulated expression of SELL, CCR7, MAL and LEF1, and upregulated expression of CCL5 (Fig. 4B) and thus were the CD27–CD4+ memory T cells in the literature (36). The CD27–CD4+ memory T cells were known to be at a more differentiated state and have stronger antigen-recall responses than their CD27+ counterparts.
- 15 PCs
- Num bins along the x-axis = 23, shape parameter = 0.8772751
- learned from the model: There are 3 well-separated clusters in 2D, but if look at the model in high-D space, the three clusters are much closer. Also, there is some continuity within the clustering structure and it didn't capture well. Therefore UMAP with n:neighbour 30 is not a good representation for this data set.
- The most important parameter is n\_neighbors - the number of approximate nearest neighbors used to construct the initial high-dimensional graph. It effectively controls how UMAP balances local versus global structure - low values will push UMAP to focus more on local structure by constraining the number of neighboring points considered when analyzing the data in high dimensions, while high values will push UMAP towards representing the big-picture structure while losing fine detail.
- The second parameter we'll investigate is min\_dist, or the minimum distance between points in low-dimensional space. This parameter controls how tightly UMAP clumps points together, with low values leading to more tightly packed embeddings. Larger values of min\_dist will make UMAP pack points together more loosely, focusing instead on the preservation of the broad topological structure.
- The third parameter is metric. This parameter plays a crucial role in determining how distances are computed within the ambient space of the input data (The term “ambient space” refers to the original or initial space in which the data exists before any transformation or dimensionality reduction).
- If it is completely a mess, then that is also further evidence that the fit is poor in high-dimensions.

### 4.3 Approach followed

- First, referred to [Chen et al. \(2023\)](#) paper which shows UMAP representation of PBMC3k data with 15 PCs and parameter choice of n:neighbor:30, min\_dist:0.1, metric:cosine.
- Observed that there are three well-separated clusters.
- Second, visualise the 15 PCs in high-dimensional space with our model and investigate whether I can see the three well-separated clusters or is it showing something different than what I saw in UMAP view suggested by the author.
- Learned from the model: Yes, it's different. There are three clusters but they are really close to each other. Also, in the largest cluster, observed non-linear continuity structure, which didn't capture by the author's UMAP representation.
- Learned from the data: Visualise with detour and colored the clusters in high-D. Identified more than three clusters which is surprising.
- In that case, need to suggest a better UMAP representation than author's suggestion.
- To find a better UMAP representation, I need to investigate different parameter choices for UMAP (or need to try another NLDR technique, but here my objective is to suggest the best parameter choice with UMAP).
- Therefore, I fitted our model for different UMAP parameter choices, record the error, and selected the parameter choice that gives the lowest error which is n:neighbor:5, min\_dist:0.99, metric:cosine.
- Then, construct our model for this UMAP data (n:neighbor:5, min\_dist:0.99, metric:cosine).
- In this representation, you can see that the clusters are closer, and the continuity of clusters are there.
- Also, what missed from looking at high-D data with detour, in this UMAP representation I can see more than three clusters.
- Then, need to check how correct am I identify the clusters in 2D and is that matched that I identify in high-D.
- Generate a confusion matrix.

### 4.4 Story

- UMAP representation of PBMC3k data with 15 PCs and parameter choice of n:neighbor:30, min\_dist:0.1, metric:cosine (author's suggestion) shows three well-separated clusters (see [Figure 8](#)). The question we need to answer is: Does this UMAP representation preserve the actual data structure, or is something missing or misidentified or misleading?

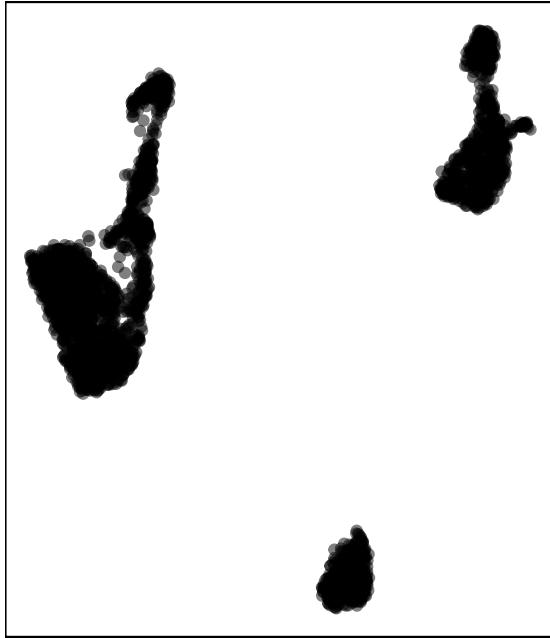


Figure 8: (a) 2D layout from UMAP ( $n_{\text{neighbors}} = 30$ ,  $\text{min\_dist} = 0.3$ ) applied for the PBMC3k dataset. Is this a best representation of the original data?

- To investigate this, we are going to visualise the model in the data space, which means that the model generated from UMAP is visualised in high-D with original data.
- To fit the model, first we need to decide how many number bins should allocate along the x and y axes. To make an initial choice, we use MSE plot (Figure 9 (b)).
- Then, the model is constructed by following all the steps in 2D and lifts the model into high-D.

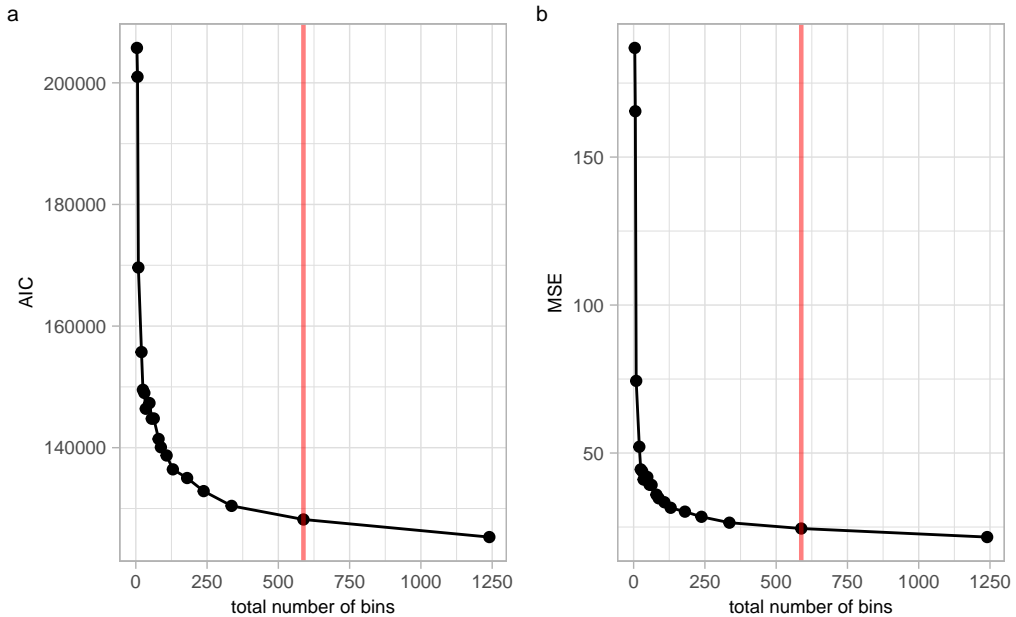


Figure 9: Goodness of fit statistics from UMAP applied to training PBMC3k dataset. What is the effective number of bins in each NLDLR technique to create a 2D model? The MSE plot have a steep slope at the beginning, indicating that a smaller number of bins causes a larger amount of error. Then, the slope gradually declines or level off, indicating that a higher number of bins generates a smaller error. Using the elbow method, when the total number of bins is set to 588, the slope of the Mean Squared Error (MSE) plot experiences a sudden and noticeable change, resembling an elbow-like shape. This point indicates that adding less bins does not enough to capture the data structure.

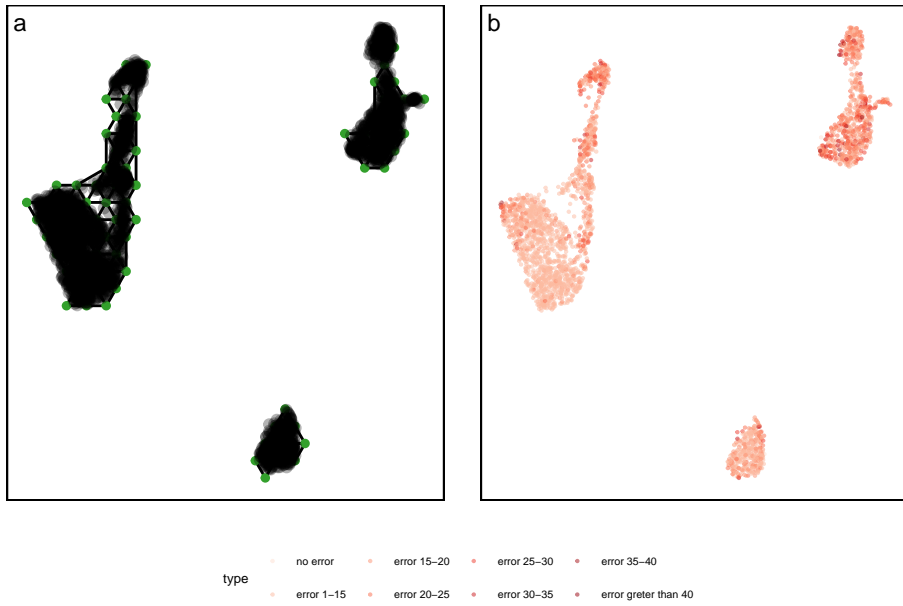


Figure 10: (a) Model in the 2D space overlaid on UMAP data, and (b) Error occurred by the high-D model for high-D data and the error mapped into 2D NLDR points.

- As shown in Figure 10, there are three well-separated clusters (according to the model in 2D space).

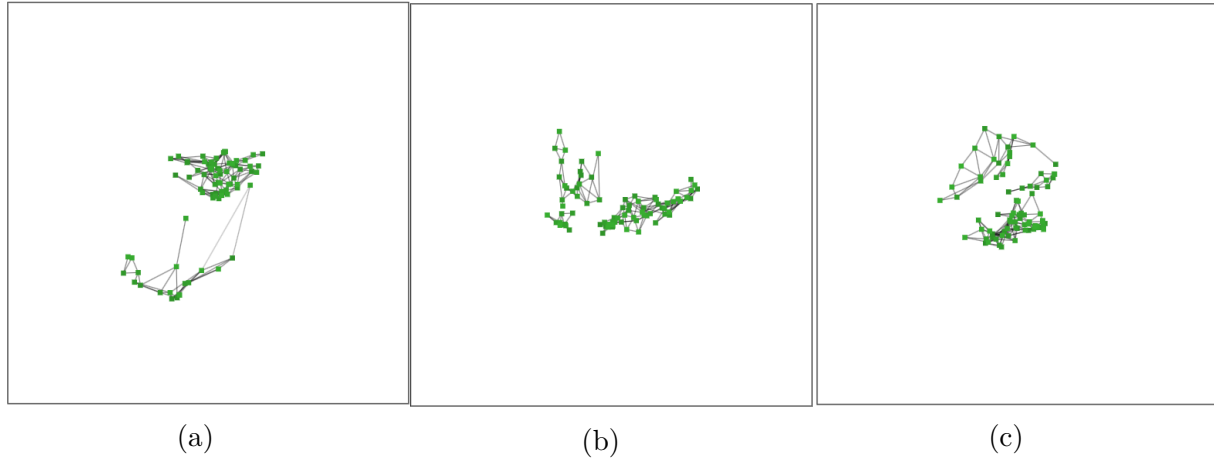


Figure 11: Screen shots of the **langevitour** of the PBMC3k data set, shows the model in high-D, a video of the tour animation is available at (<https://youtu.be/Gnhh4hfsbbg>).

- According to Figure 11 (a), the model in high-D space shows two well separated clusters. Also, two clusters are really close to each other (see Figure 11 (b)). Furthermore, there are three clusters shown by the model in 2D actually represented in high-D as well (see Figure 11 (c)). Another important thing to notice from the model in high-D space is that the non-linear continuity structure in two well-separated clusters.
- Figure 11 (c) gives evidence that UMAP preserves the global structure. Furthermore, the non-linearity within the clusters shown in Figure 11 (a) proves that local structure is also preserved but that's not visually shown by the UMAP layout in 2D.

- Can we find a better parameter choice for UMAP which shows this non-linear continuity of the big clusters in 2D space as well?
- To do that, we are going to fit models for different parameter choice and select the one which have the lowest model error in high-D (see `?@tbl-errordiffcomb`).

Table 1: errors for different parameter combinations

<b>n_neighbors</b>	<b>min_dist</b>	<b>metric</b>	<b>error (x 100)</b>
5	0.99	cosine	262.18
15	0.99	cosine	279.49
84	0.99	cosine	295.64
5	0.30	cosine	303.90
15	0.30	cosine	308.97
84	0.30	cosine	319.59
<b>30</b>	<b>0.30</b>	<b>cosine</b>	<b>386.35</b>

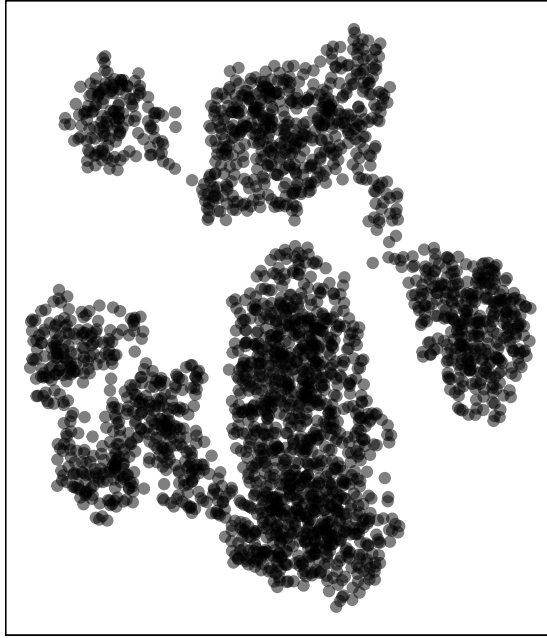


Figure 12: (a) 2D layout from UMAP ( $n\_neighbors = 5$ ,  $min\_dist = 0.99$ ,  $metric = \text{cosine}$ ) applied for the PBMC3k dataset. Is this a best representation of the original data?

- Selected the one with  $n:\text{neighbor}:5$ ,  $\text{min\_dist}:0.99$ ,  $\text{metric}:\text{cosine}$  (see Figure 12). As shown in Figure 12, the two big clusters have non-linear continuity structures, two big clusters are well-separated but close to each other, and the two cluster which exists in the one big cluster are really close to each other (see Figure 12).
- Now, we are going to fit the model for the new parameter choice.

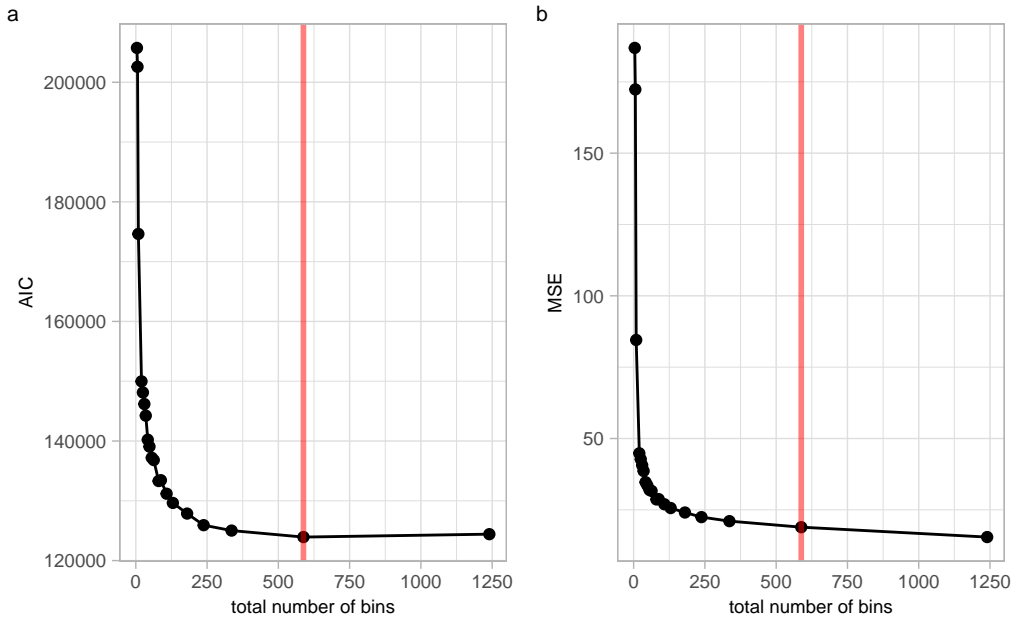


Figure 13: Goodness of fit statistics from UMAP applied to training S-curve dataset. What is the effective number of bins in each NLDR technique to create a 2D model? The MSE plot have a steep slope at the beginning, indicating that a smaller number of bins causes a larger amount of error. Then, the slope gradually declines or level off, indicating that a higher number of bins generates a smaller error. Using the elbow method, when the total number of bins is set to 588, the slope of the Mean Squared Error (MSE) plot experiences a sudden and noticeable change, resembling an elbow-like shape. This point indicates that adding less bins does not enough to capture the data structure.

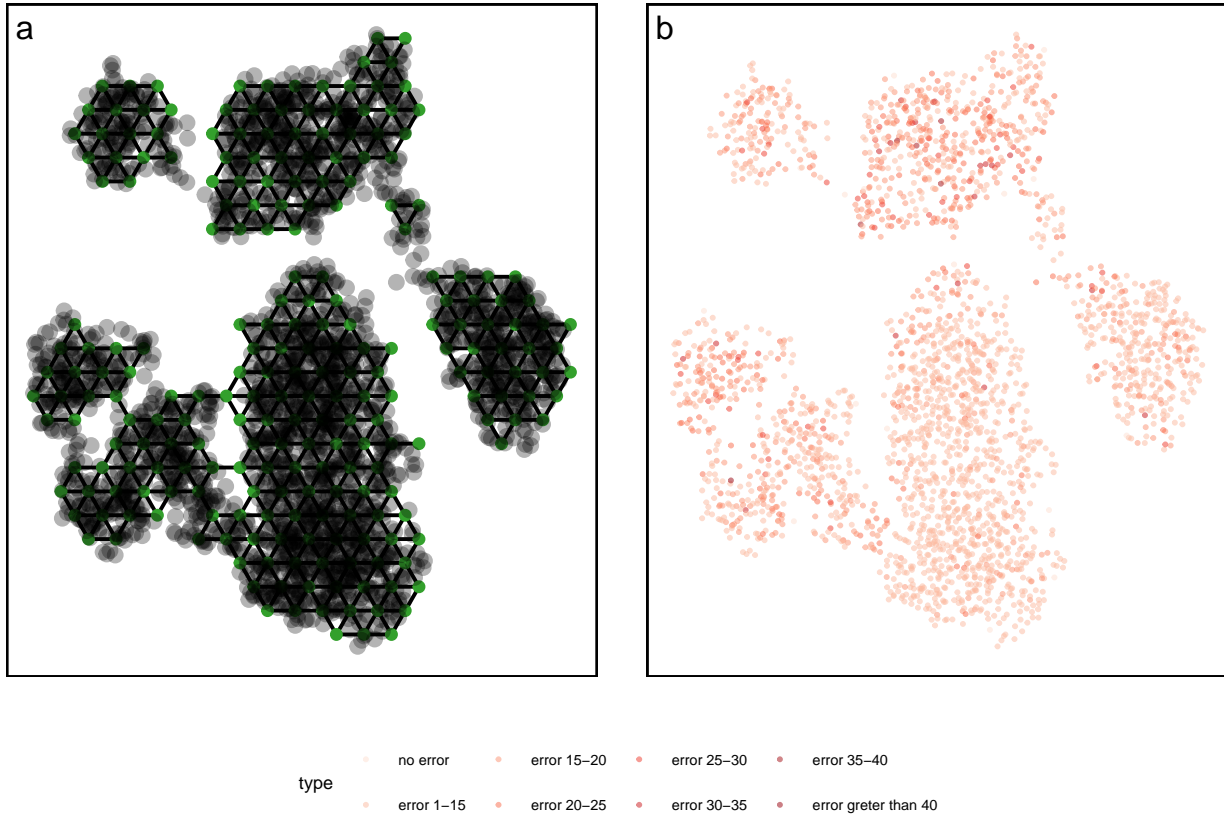


Figure 14: (a) Model in the 2D space overlaid with UMAP data, and (b) Error occurred by the high-D model for high-D data and the error mapped into 2D NLDR points.

- According to Figure 14 (a), the model constructed in 2D space for the new parameter choice of UMAP shows 5 clusters which are really close to each other. The big cluster shows the non-linear continuity structure with two sub clusters. Other three clusters positioned in a structure of non-linearity but really close to each other.

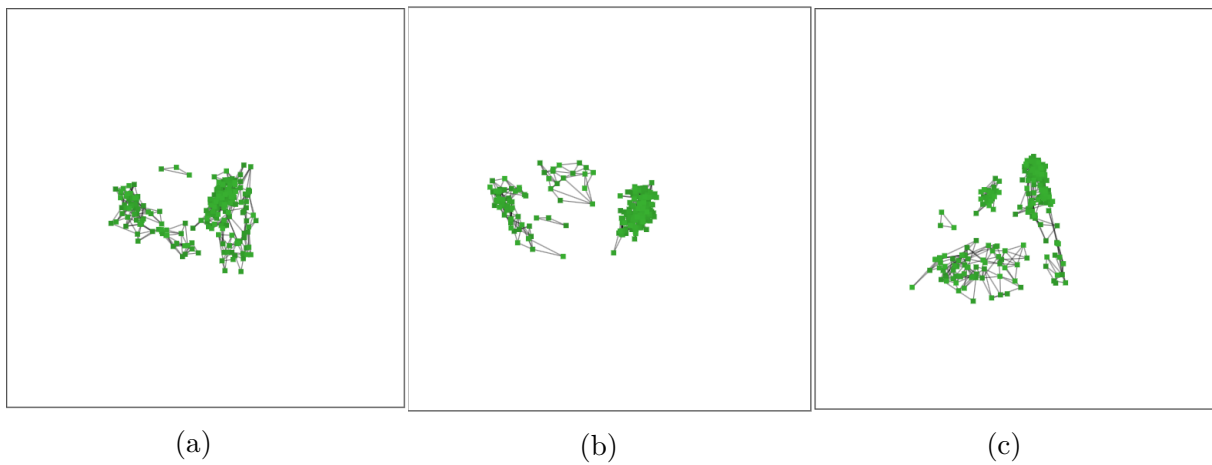


Figure 15: Screen shots of the **langevitour** of the PBMC3k data set, shows the model in high-D with new parameter choice for UMAP, a video of the tour animation is available at ([https://youtu.be/lc\\_6-rIuNHI](https://youtu.be/lc_6-rIuNHI)).

- As shown in Figure 15, there are 5 clusters, three of them are well-separated but close to each other as seen in Figure 14 (a). Also, other two clusters are really close to each other but separated from the early mentioned three clusters.
- Next, we are going to investigate whether, the clusters we identified in 2D UMAP layout, can also be identified in high-D as well.
- First, I colored the clusters in 2D layout manually. Then, I used spin-and-brush approach with `detour` to color the clusters in high-D.

	cluster 1	cluster 2	cluster 3	cluster 4	cluster 5	cluster 6
cluster 1	138	13	0	0	0	0
cluster 2	11	509	0	1	0	0
cluster 3	1	0	348	1	0	1
cluster 4	0	0	3	1029	64	2
cluster 5	0	0	0	85	226	32
cluster 6	0	0	0	0	19	139

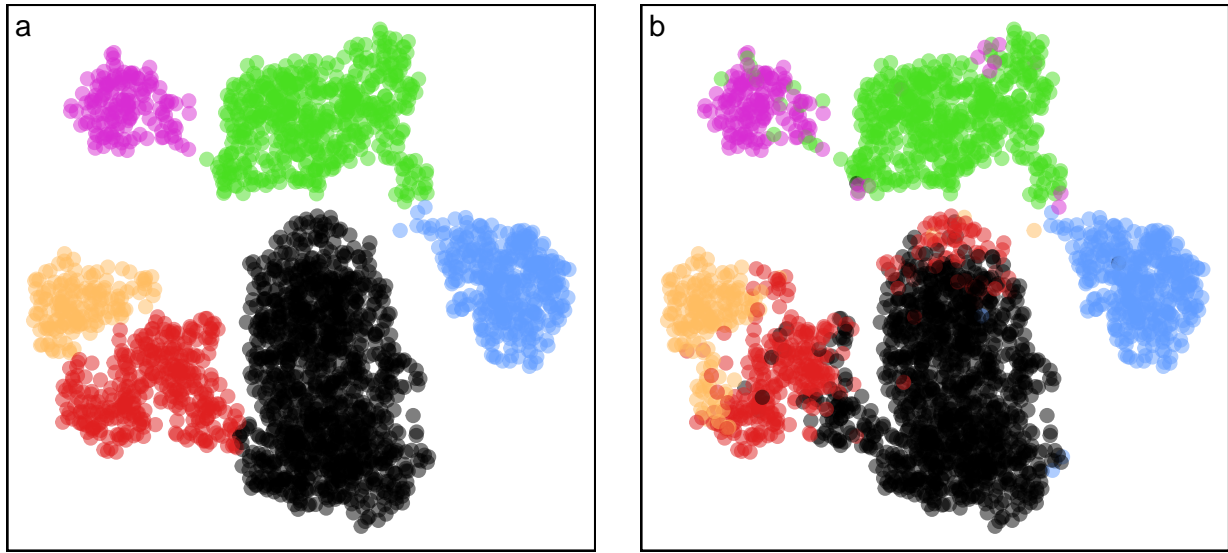
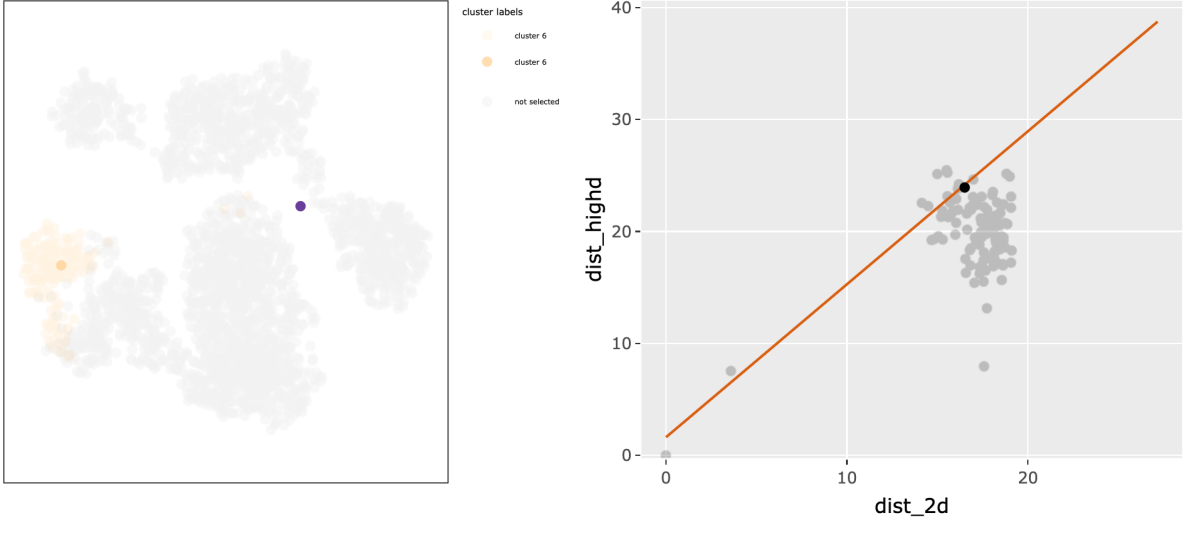


Figure 16: 2D layout from UMAP (`n_neighbors = 5`, `min_dist = 0.99`, `metric = cosine`) applied for PBMC3k dataset (a) colored manually in 2D, (b) colored in high-D.

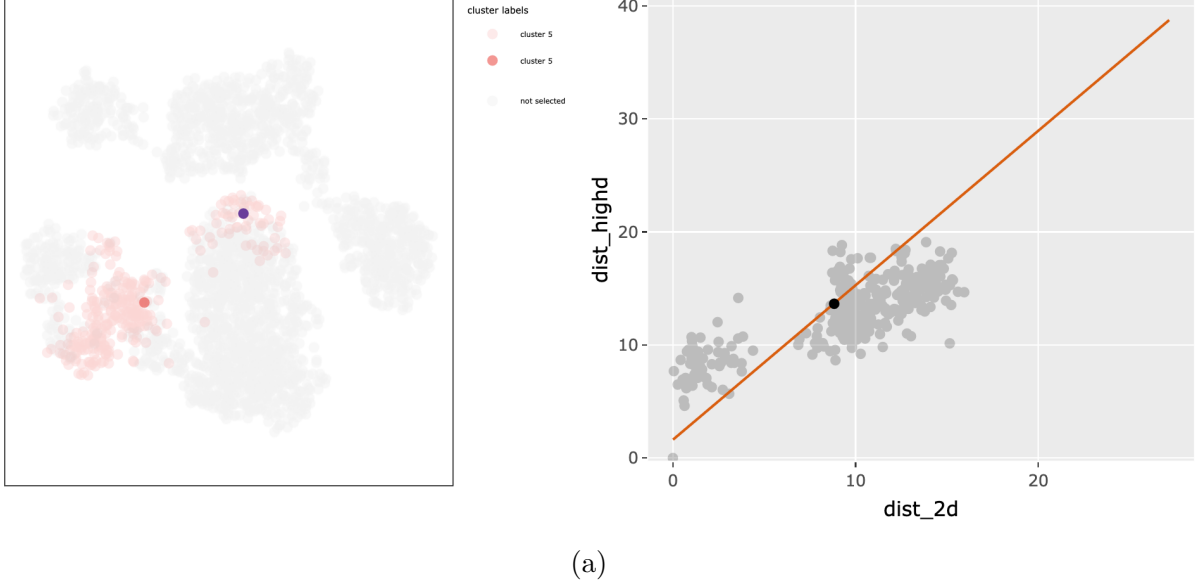
- Figure 16 shows the 2D UMAP layout colored with each method. As shown in Figure 16 (b) and the confusion matrix, there are some miss-classifications. What is the reason for that?
- For example, the point (ID: 1158) classified as **cluster 3** in 2D UMAP layout, classified as **cluster 6** when doing the colouring in high-D (see Figure 16). Why?



(a)

Figure 17: Screen shots of app which shows 2D UMAP layout and comparison of distances related to the point classified as **cluster 6** in high-D (ID: 1158) and randomly selected point which is in **cluster 6** (ID: 2291).

- If we compute the distance between these two points, you will see that it preserves the pair-wise distance (see Figure 17), which give us a evidence that even though the point 1158, classified as **cluster 3** in 2D layout, actually should be in **cluster 6**. This also evident that some misleading can happens with UMAP.



(a)

Figure 18: Screen shots of app which shows 2D UMAP layout and comparison of distances related to the point classified as **cluster 5** in high-D (ID: 3) and randomly selected point which is in **cluster 5** (ID: 2198).

- For another example, if we compute the distance between these two points, you will see that it preserves the pair-wise distance (see Figure 18), which give us a evidence that even though the point 3, classified as **cluster 4** in 2D layout, actually should be in **cluster 5**. This also evident that some misleading can happens with UMAP.

## 4.5 Handwritten digits

- Why I choose this data set? Because I need show that whatever NLDR technique that we use, our model can capture the non-linear structure within clusters as well.
- Digit 1 (7877 images only)

### 4.5.1 Preprocessing

- Scale the pixel values to the range [0,1]
- Reshape to have a 2-dimensional array
- reshaping pixel data is a fundamental preprocessing step in image analysis tasks, ensuring that the data is in a suitable format for further analysis, modeling, and interpretation. It helps preserve important spatial information, ensures compatibility with machine learning models, and facilitates feature extraction and visualization.
- Reshaping the pixel data allows us to preserve this spatial information, ensuring that the relationships between neighboring pixels are maintained.
- Many machine learning algorithms, including neural networks, expect input data to be in a specific format. For image data, this typically means a two-dimensional array where each row represents a single sample (image), and each column represents a feature (pixel value). Reshaping ensures that all samples have consistent dimensions, making them suitable for feeding into these algorithms.
- Reshaping the pixel data allows for easier extraction of relevant features from the images. Once reshaped, individual pixels can be treated as features, making it easier to apply techniques like dimensionality reduction (e.g., PCA) or feature engineering to extract meaningful information from the images.
- Selected 10 PCs based on scree plot
- 7877 images of digit 1
- PaCMAP parameters: n\_components=2, n\_neighbors=10, init="random", MN\_ratio=0.9, FP\_ratio=2.0

### 4.5.2 Model

- Total number of bins used: 180 (num\_x = 12, num\_y = 15, hex\_size = 0.06)
- Learned from the model: There is a non-linear shape in 2D, but if look at the model in high-D, the non-linear continuity is there but there is a twist in the structure which didn't capture by PaCMAP in 2D layout.

#### 4.5.3 Story

- PaCMAP representation of MNIST digit 1 data with 10PCs and parameter choice of `n_components=2`, `n_neighbors=10`, `init="random"`, `MN_ratio=0.9`, `FP_ratio=2.0` shows a non-linear structure (see Figure 20 (a)). I selected this parameter choice because this the default parameter setting for PaCMAP and selected PaCMAP because when I observed the 5 NLDR techniques applied for the data PaCMAP showed the non-linear structure effectively in 2D.
- By looking at MSE plot, I selected the 180 bins, which associated with 12 bins along the x-axis, 15 bins along the y-axis, and hex size as 0.06 (Figure 19 (b)). Then, fitted the model in 2D (see Figure 20 (b)). As you can see in Figure 20 (b), the fitted model capture the non-linear structure of the 2D data.

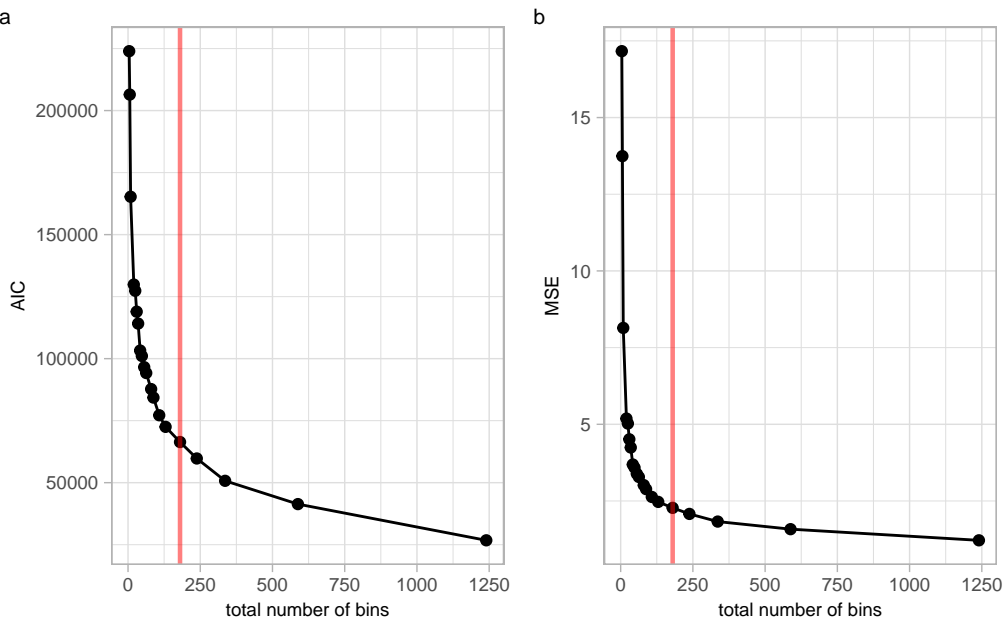


Figure 19: Goodness of fit statistics from PaCMAP applied to training MNIST dataset. What is the effective number of bins in each NLDR technique to create a 2D model? The MSE plot have a steep slope at the beginning, indicating that a smaller number of bins causes a larger amount of error. Then, the slope gradually declines or level off, indicating that a higher number of bins generates a smaller error. Using the elbow method, when the total number of bins is set to 180, the slope of the Mean Squared Error (MSE) plot experiences a sudden and noticeable change, resembling an elbow-like shape. This point indicates that adding less bins does not enough to capture the data structure.

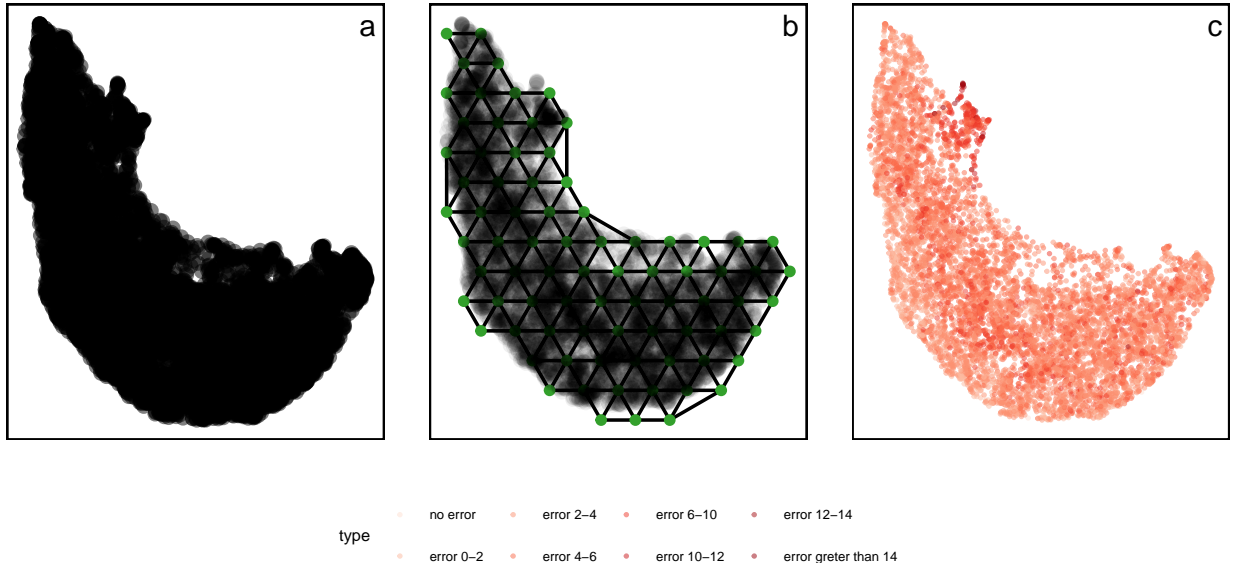


Figure 20: (a) 2D layout from PaCMAP ( $n\_components=2$ ,  $n\_neighbors=10$ ,  $init=random$ ,  $MN\_ratio=0.9$ ,  $FP\_ratio=2.0$ ) applied for the digit 1 of the MNIST dataset, (b) Model in the 2D space overlaid on PaCMAP data, and (c) Error occurred by the high-D model for high-D data and the error mapped into 2D NLDR points.

- Next, the constructed 2D model lifts into high-dimensions (see Figure 21).

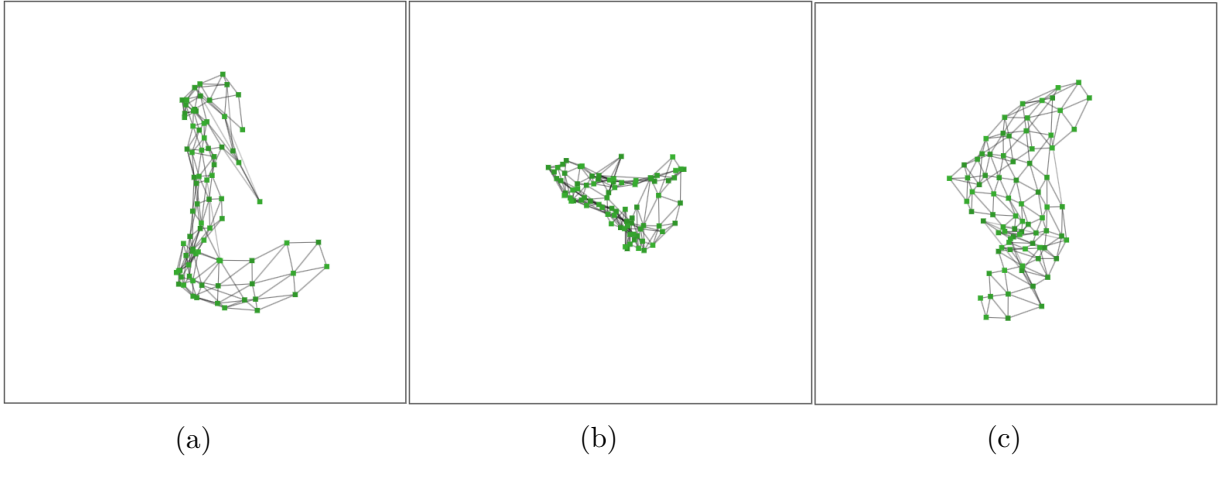


Figure 21: Screen shots of the **langevitour** of the MNIST digit 1 data set, shows the model in high-D, a video of the tour animation is available at (<https://youtu.be/zq2GM9qvUNA>).

- As shown in Figure 21 (a), the non-linear continuity structure that you have seen in 2D representation of PaCMAP, also can be seen in the model in high-D space as well. This gives us an evidence that our model capture the non-linear structure of the data effectively.
- Furthermore, our model shows some addition pattern of data which couldn't be seen in the 2D layout.
- One is the twisted structure within the non-linear structure (see Figure 21 (c)).
- Another thing is the connected corners of the non-linear structure (see Figure 21 (b)). The non-linear curve is bended.
- To gives the evidence that PaCMAP preserve the local structure (non-linear pattern), our model helps by computing the model errors (Figure 19 (c)).



Figure 22: Images of handwritten digit 1 which occur large model error.

- As you can see in Figure 19 (c), the largest model error shows in the upper right side of the 2D layout. A sample of the images that shows the largest error can be seen in Figure 22. The reason for the large model error is that the high-D points related to this largest error located away from the high-D model points.

## 5 Conclusion

In conclusion, our proposed model offers a novel approach for visualizing high-dimensional (high-D) data by leveraging non-linear dimension reduction (NLDR) techniques. Through a series of steps including hexagonating NLDR data, triangulating bin centroids, and lifting the 2D triangular mesh into high dimensions, our model effectively transforms complex high-D data into interpretable 2D representations. The model's performance is evaluated using goodness of fit statistics such as Mean Squared Error (MSE) and Akaike Information Criterion (AIC), providing insights into its accuracy and reliability. Overall, our model presents a valuable tool for researchers and practitioners in various fields to gain deeper insights from high-dimensional datasets.

Our algorithm mainly consists...

These Goodness of fit statistics useful in encountering the prediction accuracy when we predict the 2D embedding for the new high-D data. Because, we try to find the nearest high-D mappings as the first step of prediction which will participate the prediction process. When we need to find which different NLDR technique and which parameter choices is giving the best representation of high-D data, MSE and AIC are also useful.

We introduce a new tool to help to determine which method, which parameter choice provide the most useful representation of high-D data.

## References

- Amid, E. & Warmuth, M. K. (2022), ‘Trimap: Large-scale dimensionality reduction using triplets’.
- Asimov, D. (1985), ‘The grand tour: A tool for viewing multidimensional data’, *SIAM Journal on Scientific and Statistical Computing* **6**(1), 128–143.  
**URL:** <https://doi.org/10.1137/0906011>
- Ayesha, S., Hanif, M. K. & Talib, R. (2020), ‘Overview and comparative study of dimensionality reduction techniques for high dimensional data’, *Information Fusion* **59**, 44–58.
- Buja, A., Cook, D. & Swayne, D. F. (1996), ‘Interactive high-dimensional data visualization’, *Journal of Computational and Graphical Statistics* **5**(1), 78–99.  
**URL:** <http://www.jstor.org/stable/1390754>
- Carr, D. B. (1992), Looking at large data sets using binned data plots.
- Carr, D. B., Littlefield, R. J., Nicholson, W. L. & Littlefield, J. S. (1987), ‘Scatterplot matrix techniques for large n’, *Journal of the American Statistical Association* **82**(398), 424–436.  
**URL:** <http://www.jstor.org/stable/2289444>
- Carr, D., Olsen, A. & White, D. (2013), ‘Hexagon mosaic maps for display of univariate and bivariate geographical data’, *Cartography and Geographic Information Systems* **19**, 228–236.
- Carr, D., ported by Nicholas Lewin-Koh, Maechler, M. & contains copies of lattice functions written by Deepayan Sarkar (2023), *hexbin: Hexagonal Binning Routines*. R package version 1.28.3.  
**URL:** <https://CRAN.R-project.org/package=hexbin>
- Chen, Z., Wang, C., Huang, S., Shi, Y. & Xi, R. (2023), ‘Directly selecting differentially expressed genes for single-cell clustering analyses’, *bioRxiv*.  
**URL:** <https://www.biorxiv.org/content/early/2023/07/29/2023.07.26.550670>
- Coifman, R., Lafon, S., Lee, A., Maggioni, M., Nadler, B., Warner, F. & Zucker, S. (2005), ‘Geometric diffusions as a tool for harmonic analysis and structure definition of data: Diffusion maps’, *Proceedings of the National Academy of Sciences of the United States of America* **102**, 7426–31.
- Cook, D., Buja, A., Cabrera, J. & Hurley, C. (1995), ‘Grand tour and projection pursuit’, *Journal of Computational and Graphical Statistics* **4**(3), 155–172.  
**URL:** <https://www.tandfonline.com/doi/abs/10.1080/10618600.1995.10474674>
- F.R.S., K. P. (1901), ‘Liii. on lines and planes of closest fit to systems of points in space’, *The London, Edinburgh, and Dublin Philosophical Magazine and Journal of Science*

**2**(11), 559–572.

**URL:** <https://doi.org/10.1080/14786440109462720>

Guo, B., Huuki-Myers, L. A., Grant-Peters, M., Collado-Torres, L. & Hicks, S. C. (2023), ‘escheR: Unified multi-dimensional visualizations with Gestalt principles’, *bioRxiv* . Publisher: Cold Spring Harbor Laboratory \_eprint: <https://www.biorxiv.org/content/early/2023/06/08/2023.03.18.533302.full.pdf>.

**URL:** <https://www.biorxiv.org/content/early/2023/06/08/2023.03.18.533302>

Hao, Y., Hao, S., Andersen-Nissen, E., III, W. M. M., Zheng, S., Butler, A., Lee, M. J., Wilk, A. J., Darby, C., Zagar, M., Hoffman, P., Stoeckius, M., Papalex, E., Mimitou, E. P., Jain, J., Srivastava, A., Stuart, T., Fleming, L. B., Yeung, B., Rogers, A. J., McElrath, J. M., Blish, C. A., Gottardo, R., Smibert, P. & Satija, R. (2021), ‘Integrated analysis of multimodal single-cell data’, *Cell* .

**URL:** <https://doi.org/10.1016/j.cell.2021.04.048>

Hart, C. & Wang, E. (2022), *detourr: Portable and Performant Tour Animations*. R package version 0.1.0.

**URL:** <https://casperhart.github.io/detourr/>

Howley, T., Madden, M., O’Connell, M.-L. & Ryder, A. (2005), The effect of principal component analysis on machine learning accuracy with high dimensional spectral data, pp. 209–222.

Indhumathi, R. & Sathiyabama, S. (2010), ‘Reducing and clustering high dimensional data through principal component analysis’, *International Journal of Computer Applications* **11**(8), 1–4.

Jia, W., Sun, M., Lian, J. & Hou, S. (2022), ‘Feature dimensionality reduction: a review’, *Complex & Intelligent Systems* **8**(3), 2663–2693.

**URL:** <https://doi.org/10.1007/s40747-021-00637-x>

Johnstone, I. M. & Titterington, D. M. (2009), ‘Statistical challenges of high-dimensional data’, *Philosophical Transactions of the Royal Society A: Mathematical, Physical and Engineering Sciences* **367**(1906), 4237–4253.

**URL:** <https://royalsocietypublishing.org/doi/abs/10.1098/rsta.2009.0159>

Jolliffe, I. T. & Cadima, J. (2016), ‘Principal component analysis: a review and recent developments’, *Philosophical Transactions of the Royal Society A: Mathematical, Physical and Engineering Sciences* **374**(2065), 20150202.

**URL:** <https://royalsocietypublishing.org/doi/abs/10.1098/rsta.2015.0202>

Kruskal, J. B. (1964), ‘Nonmetric multidimensional scaling: a numerical method’, *Psychometrika* **29**(2), 115–129.

Lee, D. T. & Schachter, B. J. (1980), ‘Two algorithms for constructing a Delaunay triangulation’, *International Journal of Computer & Information Sciences* **9**(3), 219–242.

**URL:** <https://doi.org/10.1007/BF00977785>

Lee, S., Laa, U. & Cook, D. (2020), ‘Casting multiple shadows: High-dimensional interac-

tive data visualisation with tours and embeddings’.

**URL:** <https://arxiv.org/abs/2012.06077>

Liao, Y.-T., Luo, H. & Ma, A. (2023), ‘Efficient and robust bayesian selection of hyperparameters in dimension reduction for visualization’.

Lloyd, E. L. (1977), On triangulations of a set of points in the plane, *in* ‘18th Annual Symposium on Foundations of Computer Science (sfcs 1977)’, pp. 228–240.

McInnes, L. & Healy, J. (2018), ‘Umap: Uniform manifold approximation and projection for dimension reduction’, *ArXiv abs/1802.03426*.

Moon, K. R., van Dijk, D., Wang, Z., Gigante, S. A., Burkhardt, D. B., Chen, W. S., Yim, K., van den Elzen, A., Hirn, M. J., Coifman, R. R., Ivanova, N. B., Wolf, G. & Krishnaswamy, S. (2019), ‘Visualizing structure and transitions in high-dimensional biological data’, *Nature Biotechnology* **37**, 1482 – 1492.

Paul Harrison (2022), ‘langevitour: smooth interactive touring of high dimensions, demonstrated with scRNA-Seq data’, *bioRxiv* p. 2022.08.24.505207.

**URL:** <http://biorkxiv.org/content/early/2022/08/26/2022.08.24.505207.abstract>

Renka, R. J. (1996), ‘Algorithm 751: Tripack: A constrained two-dimensional delaunay triangulation package’, *ACM Trans. Math. Softw.* **22**(1), 1–8.

**URL:** <https://doi.org/10.1145/225545.225546>

Rumelhart, D. E., Hinton, G. E. & Williams, R. J. (1986), ‘Learning representations by back-propagating errors’, *Nature* **323**, 533–536.

Satija, R., Hoffman, P. & Butler, A. (2019), *SeuratData: Install and Manage Seurat Datasets*. <http://www.satijalab.org/seurat>, <https://github.com/satijalab/seurat-data>.

Silva, V. & Tenenbaum, J. (2002), ‘Global versus local methods in nonlinear dimensionality reduction’, *Advances in neural information processing systems* **15**.

Swayne, D. F., Cook, D. & Buja, A. (1998), ‘Xgobi: Interactive dynamic data visualization in the x window system’, *Journal of Computational and Graphical Statistics* **7**(1), 113–130.

**URL:** <http://www.jstor.org/stable/1390772>

Torgerson, W. S. (1967), *Theory and methods of scaling*, Wiley New York.

van der Maaten, L. & Hinton, G. E. (2008), ‘Visualizing data using t-sne’, *Journal of Machine Learning Research* **9**, 2579–2605.

Wang, Y., Huang, H., Rudin, C. & Shaposhnik, Y. (2021), ‘Understanding how dimension reduction tools work: An empirical approach to deciphering t-sne, umap, trimap, and pacmap for data visualization’, *Journal of Machine Learning Research* **22**(201), 1–73.

**URL:** <http://jmlr.org/papers/v22/20-1061.html>

Wickham, H., Cook, D. & Hofmann, H. (2015), ‘Visualizing statistical models: Removing the blindfold’, *Statistical Analysis and Data Mining: The ASA Data Science Journal* **8**(4), 203–225.

**URL:** <https://onlinelibrary.wiley.com/doi/abs/10.1002/sam.11271>

Wickham, H., Cook, D., Hofmann, H. & Buja, A. (2011), ‘tourr: An r package for exploring multivariate data with projections’, *Journal of Statistical Software* **40**(2), 1–18.  
**URL:** <http://www.jstatsoft.org/v40/i02/>